Antiferromagnetism and Phase Stability of CrMnFeCoNi High-Entropy Alloy

Zhu, Li; He, Haiyan; Naeem, Muhammad; Sun, Xun; Qi, Ji; Liu, Peng; Harjo, Stefanus; Nakajima, Kenji; Li, Bing; Wang, Xun-Li

Published in:
Physical Review Letters

Published: 20/09/2024

Document Version:
Final Published version, also known as Publisher's PDF, Publisher's Final version or Version of Record

Published version (DOI):
10.1103/PhysRevLett.133.126701

Publication details:
Zhu, L., He, H., Naeem, M., Sun, X., Qi, J., Liu, P., Harjo, S., Nakajima, K., Li, B., & Wang, X.-L. (2024). Antiferromagnetism and Phase Stability of CrMnFeCoNi High-Entropy Alloy. *Physical Review Letters*, *133*(12), Article 126701. https://doi.org/10.1103/PhysRevLett.133.126701

Antiferromagnetism and Phase Stability of CrMnFeCoNi High-Entropy Alloy

Li Zhu,[1,2,*] Haiyan He,[1,3,4,*] Muhammad Naeem,[1,5,*] Xun Sun,[1,2] Ji Qi,[6] Peng Liu,[6] Stefanus Harjo,[7] Kenji Nakajima,[7] Bing Li,[6,†] and Xun-Li Wang[1,2,‡]

[1]*Department of Physics and Center for Neutron Scattering, City University of Hong Kong, 83 Tat Chee Avenue, Kowloon, Hong Kong*

[2]*City University of Hong Kong Shenzhen Research Institute, 8 Yuexing 1st Road, Shenzhen Hi-Tech Industrial Park, Shenzhen 518057, China*

[3]*School of Physical Sciences, Great Bay University, Dongguan 523000, China*

[4]*Great Bay Institute for Advanced Study, Dongguan 523000, China*

[5]*School of Metallurgy and Materials, University of Birmingham, Birmingham B15 2TT, United Kingdom*

[6]*Shenyang National Laboratory for Materials Science, Institute of Metal Research, Chinese Academy of Sciences, Shenyang 110016, China*

[7]*J-PARC Center, Japan Atomic Energy Agency, Tokai, Ibaraki 319-1195, Japan*

(Received 16 August 2023; revised 5 August 2024; accepted 9 August 2024; published 17 September 2024)

It has long been suspected that magnetism could play a vital role in the phase stability of multicomponent high-entropy alloys. However, the nature of the magnetic order, if any, has remained elusive. Here, by using elastic and inelastic neutron scattering, we demonstrate evidence of antiferromagnetic order below ~80 K and strong spin fluctuations persisting to room temperature in a single-phase face-centered cubic (fcc) CrMnFeCoNi high-entropy alloy. Despite the chemical complexity, the magnetic structure in CrMnFeCoNi can be described as γ-Mn-like, with the magnetic moments confined in alternating (001) planes and pointing toward the $\langle 111 \rangle$ direction. Combined with first-principles calculation results, it is shown that the antiferromagnetic order and spin fluctuations help stabilized the fcc phase in CrMnFeCoNi high-entropy alloy.

DOI: 10.1103/PhysRevLett.133.126701

High-entropy alloys (HEAs), referring to alloys that contain multiple principal elements in near-equal atomic ratios, can form a single-phase crystal with a simple lattice [1–3]. Several criteria have been proposed to elaborate the phase selection in high-entropy alloys, such as valence electron concentration (VEC) [4], electrons per atom ratio (e/a) [5], static displacement [6], atomic-scale chemical ordering [7], and so on. However, the mechanism determining the stability of a particular phase for HEAs has not been fully understood, even for the prototypical quinary CrMnFeCoNi HEA, known as Cantor alloy [8]. Studies by electron microscopy and neutron diffraction at room temperature demonstrated that CrMnFeCoNi HEA retains its face-centered cubic (fcc) structure until fracture [9,10]. Driven by the low stacking fault energy, a quantity proportional to the Gibbs energy difference between the fcc and the hcp (hexagonal close-packed) phases, an fcc-to-hcp phase transformation during low-temperature deformation has been predicted by early first-principles calculations [11,12]. In fact, such a phase transformation has been observed in another equiatomic fcc CrCoNi alloy by our previous low-temperature *in situ* neutron diffraction experiments [13,14]. By contrast, there is no evidence of a martensitic transformation in CrMnFeCoNi HEA even down to 15 K [10,15]. These experimental observations suggested other mechanisms that stabilized the fcc phase of HEAs.

First-principles calculations have also suggested the contribution of magnetism to the stacking fault energy and phase stability in stainless steels as well as in HEAs [16–19]. Such a proposal makes sense because the magnetic ordering or exchange interactions will lower the overall Gibbs free energy. However, so far, the nature of the magnetic order in CrMnFeCoNi HEA, if any, has remained elusive and even controversial. For example, through magnetic susceptibility measurements, Schneeweiss *et al.* [20] reported a paramagnetic to spin-glass transformation at 93 K in CrMnFeCoNi HEA, while Özgün *et al.* [21] proposed and argued for antiferromagnetic ordering around 75–90 K before entering into a spin-frozen state in off-equiatomic CrMnFeCoNi alloys. An antiferromagnetic or possible spin-glass state was also suggested in the single crystal CrMnFeCoNi but at a lower temperature (i.e., 25 K) [22]. These differing experimental results call for an in-depth study of the magnetic behaviors in CrMnFeCoNi HEA at the atomistic level. Here, by employing elastic and inelastic neutron scattering, we show evidence of the

*These authors contributed equally to this letter.

†Contact author: bingli@imr.ac.cn

‡Contact author: xlwang@cityu.edu.hk

antiferromagnetic order and strong spin fluctuations in CrMnFeCoNi HEA. An antiferromagnetic structure consistent with experimental observations is proposed for the CrMnFeCoNi HEA. Taking into account the first-principles calculation results, we demonstrate that the antiferromagnetic order and spin fluctuations stabilize the fcc phase.

The CrMnFeCoNi HEA were prepared by induction melting followed by drop cast into a rectangular Cu mold. The samples were initially hot forged and then homogenized by annealing at 1473 K for 24 h under an argon atmosphere and then quenched in iced water. The chemical composition of our prepared sample was analyzed using energy-dispersive spectroscopy (EDS, JSM-IT500), revealing the stoichiometric CrMnFeCoNi and uniform element distribution (Supplemental Material, Fig. S1 and Table S1 [23]). Magnetic susceptibility was characterized using a superconductor quantum interference device magnetometer (SQUID, MPMS-XL, Quantum Design) and physical property measurement system (PPMS, Quantum Design). Two neutron diffraction experiments were conducted using the TAKUMI diffractometer at Japan Proton Accelerator Research Complex (J-PARC). In the first experiment, the sample was cooled to 10 K without load. In the second experiment, a tensile stress was applied after the temperature reached 35 K. The time-of-flight neutron diffraction data with momentum transfer Q parallel and perpendicular to the loading direction were collected simultaneously by two detector banks located at $\pm 90°$ relative to the incident neutron beam (see Fig. S2 for details [23]). In the text below, the loading and transverse directions are denoted as LD and TD, respectively. Inelastic neutron scattering measurements were performed using the cold neutron disk-chopper spectrometer AMATERAS at J-PARC [24]. The inelastic data were reduced using the Utsusemi suite and visualized in the data analysis and visualization environment (DAVE) [25]. The first-principles calculations were carried out using the exact muffin-tin orbitals (EMTO) method [26] in combination with the single-site coherent potential approximation (CPA) [27]. The Perdew-Burke-Ernzerhof formula for the generalized gradient approximation (GGA) was adopted [28]. To solve the on-electron Kohn-Sham equations, we employed the scalar-relativistic approximation and soft-core scheme. We used the disordered local moment (DLM) model to describe the paramagnetic states [29], while the antiferromagnetic states were described by the magnetic moments in alternate (001) planes being antiparallel aligned.

Our neutron diffraction data demonstrates that the CrMnFeCoNi HEA has a single-phase fcc structure over the entire investigated temperature region. As an example, the Rietveld refinement on the diffraction data collected at 293 K is displayed in Fig. 1(a). No secondary phase or impurity was detected. A peak located at around 2.54 Å appeared at low temperatures [Fig. 1(b)]. This peak can be indexed as (110), which is forbidden for nuclear scattering from an fcc structure. As will be shown below, the (110) superlattice peak manifests the magnetic scattering of an antiferromagnetically ordered structure. By plotting the normalized integrated intensity as a function of temperature [Fig. 1(c)], the onset of the ordering temperature can be determined. From the complementary dc magnetic susceptibility measurements [Fig. 1(d)], we found the transformation from paramagnetic to long-range antiferromagnetic order occurs at a Néel temperature of $T_N \sim 80$ K, consistent with the results of neutron diffraction. As shown in Fig. 1(e), the absence of frequency dependence for the cusp at ~80 K is evident, which is compatible with a long-range antiferromagnetic order and in contrast to the characteristics of a spin glass state [30]. Moreover, we fitted the neutron data using a $(1\text{-}T/T_N)^{2\beta}$ power law relation. The fitting yields a critical exponent $\beta = 0.30 \pm 0.04$, which is closer to the theoretical value of 0.33 for a 3D Ising antiferromagnet [31], rather than a Heisenberg antiferromagnet of 0.38 [32]. For comparison, no (110) magnetic peak was detected for CrCoNi alloy (Fig. S3 [23]). Following Ishikawa *et al.*'s studies on FeNiCr and FeMn alloys [33,34], we propose an antiferromagnetic structure for the CrMnFeCoNi HEA, as illustrated in Fig. 1(f). The magnetic moments in the alternate (100) planes are aligned antiparallel and point along the $\langle 111 \rangle$ direction. Later, we will provide experimental evidence supporting the proposed structure by elastic and inelastic neutron scattering measurements.

To gain further insights into the antiferromagnetism of CrMnFeCoNi HEA, the dynamic structure factors $S(Q, E)$ were determined using inelastic neutron scattering (Fig. 2) with AMATERAS. Figures 2(a) and 2(b) show experimentally determined $S(Q, E)$ as functions of the momentum and energy transfers at 6 K (the antiferromagnetic state) and 300 K (the paramagnetic state), respectively. At 300 K, excitations can be identified at Q values corresponding to (100), (110), (111), (200), and (220) Bragg positions, while only the excitation at the (100) position is prominent at 6 K. Because of the Q dependence of the magnetic form factors, the magnetic scattering intensity is more pronounced at lower Q [34,35]. In contrast, at high Q values, the scattering is dominated by phonon scattering. We also analyzed inelastic neutron scattering data of a polycrystalline Ni, a fcc metal. As expected, the scattering around the (100) position is absent for Ni, demonstrating that the excitation seen in Fig. 2 is a unique feature for the CrMnFeCoNi HEA (Fig. S4 [23]). Therefore, in the following, we will focus on the (100) scattering. It is noted that both the position and the full width at half maximum of the (100) magnetic scattering remain almost unchanged up to at least 16 meV at 6 K, indicating a high stiffness of the spin excitations. To further prove that the feature at (100) Bragg position is a result of long-wavelength magnons, we integrated the $S(Q, E)$ over a Q range of $[1.4, 2.0]$ Å^{-1}. As shown in Fig. S5 [23], the inelastic scattering intensity

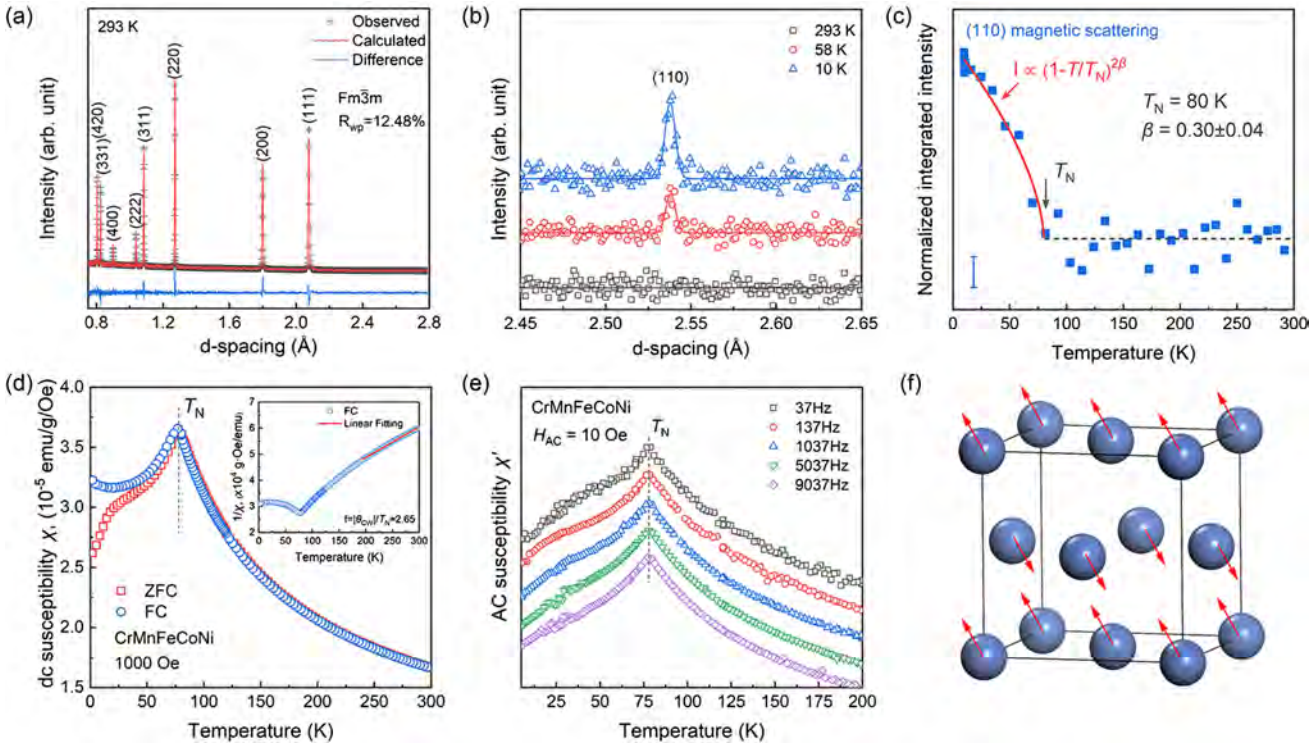

FIG. 1. Development of antiferromagnetic ordering during cooling revealed by neutron diffraction and magnetic susceptibility measurements for CrMnFeCoNi HEA. (a) Neutron diffraction pattern at 293 K and the Rietveld refinement. The peaks can be indexed with the nuclear scattering of a fcc structure (space group $Fm\bar{3}m$, $a = 3.5949 \pm 0.0002$ Å). (b) Selected diffraction patterns in the region of 2.45–2.65 Å at different temperatures to highlight the development of the (110) superlattice peak. Solid lines are Gaussian fits. (c) Normalized integrated intensities of the (110) superlattice peak as a function of temperature. The error bar is presented in the lower left corner. The red line is a fit using equation $I \propto (1\text{-}T/T_N)^{2\beta}$. (d) dc magnetic susceptibility χ versus temperature measured at a magnetic field of 1000 Oe. ZFC and FC represent measurements under zero-field cooling and field-cooling conditions, respectively. The inset is the temperature dependence of $1/\chi$; the red line is the Curie-Weiss fit. (e) Real part of ac magnetic susceptibility χ' at various frequencies upon cooling. The data have been shifted vertically for clarity. (f) The proposed magnetic structure in CrMnFeCoNi HEA, where the blue spheres represent atoms and the red arrows the direction of magnetic moments, i.e., the $\langle 111 \rangle$ direction.

at 6 K is asymmetric, which is typical for magnons. In contrast, for the spectra at 300 K, diffuse scattering features, characterized by a Lorentzian distribution centered at $E = 0$ can be readily discerned. The remarkable difference at these two representative temperatures demonstrates that strong spin fluctuations exist at 300 K, a temperature reaching approximately three times the Néel temperature T_N. Therefore, in CrMnFeCoNi HEA, the

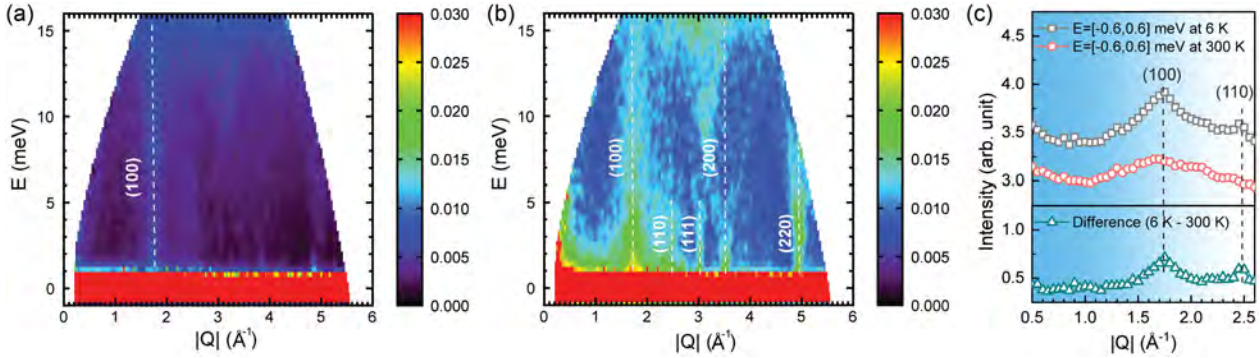

FIG. 2. Spin dynamics in CrMnFeCoNi HEA determined by inelastic neutron scattering. Color maps of the dynamic structure factor $S(Q, E)$ as functions of momentum transfer Q and energy transfer E at (a) 6 K and (b) 300 K. (c) Integrated dynamic structure factor $S(Q, E)$ over an energy transfer of $[-0.6, 0.6]$ meV to obtain the elastic scattering profile for the CrMnFeCoNi HEA at 6 K and 300 K. Bottom panel is the corresponding difference in which the (100) and (110) scatterings become more prominent. The incident neutron energy was $E_i = 21.81$ meV.

short-range magnetic correlation persists well above the T_N, a regime where the long-range antiferromagnetic order has long disappeared.

The elastic scattering component can be extracted by integrating the dynamic structure factor $S(Q,E)$ over the instrument resolution for the elastic peaks, i.e., $[-0.6, 0.6]$ meV [Fig. 2(c)]. The elastic data from AMATERAS contained structural information at smaller Q values that were not reached by TAKUMI. A broad peak located at $Q \sim 1.75$ Å^{-1}, the position of (100) magnetic scattering, was observed for the CrMnFeCoNi HEA at 6 K. There was also a small hump at $Q \sim 2.50$ Å^{-1} for the pattern at 6 K in the AMATERAS data, which disappeared at room temperature, indicating the absence of long-range antiferromagnetic order at room temperature, in agreement with the neutron diffraction data from TAKUMI. After subtracting the data at room temperature from that of 6 K, the (100) and (110) scattering intensities become more prominent [see bottom panel in Fig. 2(c)]. We then estimated the ratio of (100) integrated intensity relative to the (110), and found the value to be $\sim 4.5 \pm 0.2$.

The antiferromagnetic ordering of fcc materials has been extensively studied by Ishikawa *et al.* [33]. For these alloys, the antiferromagnetic structure can be classified into two groups, depending on whether the (100) scattering is visible. When both the (100) and (110) scatterings are visible, the magnetic moments in alternating (100) planes align antiparallel and cant with respect to the $\langle 100 \rangle$ direction. On the other hand, an antiferromagnetic structure can form in which the magnetic moments of the four atoms in the unit cell point toward the cell center or opposing $\langle 100 \rangle$ directions in alternating layers. However, for these two models, the (100) magnetic peak is forbidden (see Fig. S6 for details [23]). In our experiments, both (100) and (110) magnetic scatterings have been observed. Therefore, the magnetic moments in CrMnFeCoNi HEA are not in the $\langle 100 \rangle$ direction.

It has been shown that for a cubic polycrystalline specimen of randomly oriented grains, the direction of magnetic moments cannot be determined through neutron diffraction since any moment direction with respect to the crystallographic axis would give the same magnetic intensity [36]. However, tensile loading introduced preferred orientation, providing us an opportunity to assess the direction of the magnetic moments with the current polycrystalline sample. To illustrate, selected neutron diffraction patterns along TD at different true strains are depicted in Fig. 3(a). Bragg peaks evolve upon loading. For example, the (111) intensity along TD decreases, while the (111) peak grows in intensity along LD [Fig. 3(b)]. For a polycrystal with an fcc structure, the grains with the (111) orientation rotate toward LD during plastic deformation [37], leading to the (111) intensity increasing when the momentum transfer Q is parallel to LD. Our experimental observations are in line with the (111)||LD

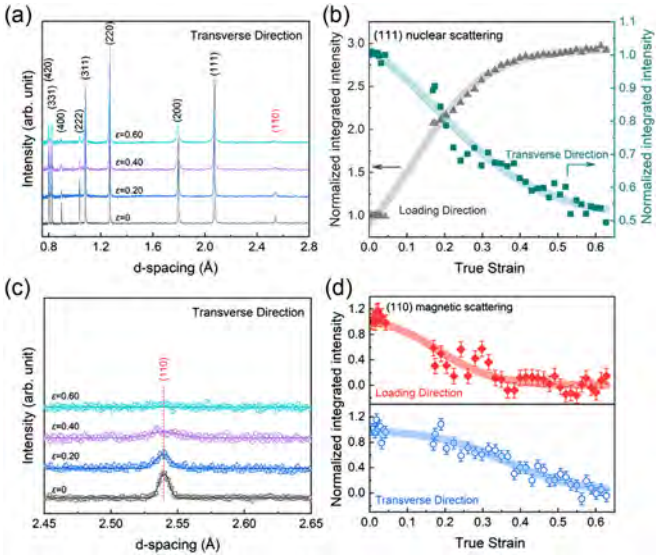

FIG. 3. Determining the direction of magnetic moments for CrMnFeCoNi HEA with the aid of preferred orientation due to tensile loading. (a) Selected diffraction patterns along TD at different strain levels at 35 K, showing the variation of diffraction peaks upon loading. (b) The normalized integrated intensities of the (111) nuclear scatterings along LD and TD normalized by the values without load as a function of true strain, showing the development of $\langle 111 \rangle$||LD texture. Note the error bar is smaller than the symbol size. (c) Selected diffraction patterns in the region of 2.45–2.65 Å along TD at different strains to highlight the magnetic (110) peak. (a) The normalized integrated intensities of (110) magnetic scattering along LD and TD as a function of true strain. That (110) decreases more quickly in LD suggests that the magnetic moment is aligned along $\langle 111 \rangle$, considering the development of the (111)||LD texture.

texture (preferred orientation) development due to dislocation slip in fcc materials. The deformation mechanism of CrMnFeCoNi HEA has been elucidated in our previous work [10]. Herebelow, we utilized the development of (111)||LD texture during deformation to determine the direction of the magnetic moments.

As shown in Fig. 3(d), the intensity of (110) along LD decreases more rapidly than that along TD. The neutron cross-section for the magnetic scattering from an antiferromagnetic alloy is given by

$$\left(\frac{d\sigma}{d\Omega}\right)_{mag} \propto [1\text{-}(\hat{\boldsymbol{\tau}}_{\mathbf{m}} \cdot \hat{\boldsymbol{\eta}})^2] |F_m(\boldsymbol{\tau}_{\mathbf{m}})|^2, \quad (1)$$

where $\hat{\boldsymbol{\tau}}_{\mathbf{m}}$ and $\hat{\boldsymbol{\eta}}$ are the unit vector in the direction of magnetic reciprocal lattice and magnetic moments, respectively, and $F_m(\boldsymbol{\tau}_{\mathbf{m}})$ is the magnetic structure factor and can be expressed as

$$F_m(\boldsymbol{\tau}_{\mathbf{m}}) = p_0 \sum_{i=1}^{n} \mu_i f_i(\boldsymbol{\tau}_{\mathbf{m}}) \sigma_d \exp(i\boldsymbol{\tau}_{\mathbf{m}} \cdot \mathbf{r}_{\mathbf{d}}) \exp(-W_d), \quad (2)$$

where p_0 is a constant equaling to 2.695×10^{-15} m, μ_i and $f_i(\boldsymbol{\tau}_\mathbf{m})$ denote the magnetic moment and magnetic form factor of atom i, respectively, σ_d has the value of ± 1, $\mathbf{r_d}$ is the position of magnetic atoms, and $\exp(-W_\mathrm{d})$ is the Debye-Wallar factor [38,39]. The $[1\text{-}(\hat{\boldsymbol{\tau}}_\mathbf{m} \cdot \hat{\boldsymbol{\eta}})^2]$ term can be expressed as $\sin^2\alpha$, where α is the angle between $\hat{\boldsymbol{\tau}}_\mathbf{m}$ and $\hat{\boldsymbol{\eta}}$. Given that the magnetic scattering occurs only when momentum transfer $\mathbf{Q} = \boldsymbol{\tau}_\mathbf{m}$, neutrons scattering is therefore insensitive to the magnetization component parallel to the momentum transfer $\mathbf{Q}$. For this reason, the development of $(111)//\mathrm{LD}$ texture during deformation would lead to a reduction of the magnetic scattering intensity in LD if the magnetic moments are parallel to the $\langle 111 \rangle$ direction, which is observed in Fig. 3(d) and Supplemental Material Fig. S6 [23]. Combining the neutron scattering results from TAKUMI and AMATERAS, we can conclude that the magnetic structure in CrMnFeCoNi HEA resembles that of γ-Mn, but with the magnetic moments pointing along the $\langle 111 \rangle$ direction [inset of Fig. 1(c)]. To further validate the proposed magnetic structure, we simulated the corresponding neutron powder diffraction pattern by GSAS-II [40] (Fig. S7 [23]), which allowed us to determine the integrated intensity ratio of $(I_{100}/I_{110})_\mathrm{cal}$. The calculated intensity ratio is ~5.2, in reasonable agreement with the experimentally determined value of 4.5 ± 0.2.

It is found that the (110) magnetic peak diminishes entirely at large strain [Fig. 3(d)], indicating that the deformation breaks down the antiferromagnetic order. This observation can be explained by considering the Bethe-Slater curve, which shows how the exchange energy varies as a function of the interatomic spacing [41]. For transition metals, the increasing lattice spacing due to tensile deformation reduces the antiferromagnetic exchange coupling, and hence the average ordered moments. As a result, the magnetic scattering intensity vanishes at large tensile deformation.

Building upon the proposed magnetic structure, we then use first-principles calculations to compare the total energy for CrMnFeCoNi HEA with various magnetic ordering and structures, i.e., fcc in the antiferromagnetic state (fcc-AFM), fcc in the ferromagnetic state (fcc-FM), fcc in the paramagnetic state (fcc-PM), together with the hcp in the paramagnetic state (hcp-PM). The first-principles calculations were carried out using the experimentally determined lattice parameter (i.e., 3.585 Å at 35 K). Figure 4 shows the calculated total energy relative to that of the hcp-PM. Consistent with previous results [12,42], the fcc-PM has relatively higher energy with respect to the fcc-PM phase, but the difference is relatively small, ~4.6 meV/atom. However, after introducing the antiferromagnetic order, the total energy for CrMnFeCoNi HEA with an fcc structure is reduced significantly, see Fig. 4. This leads to the lowest energy state for the fcc-AFM. The calculated total energies can account for the absence of martensitic transformation in CrMnFeCoNi HEA and demonstrate the significance of antiferromagnetic order in stabilizing the fcc phase. By

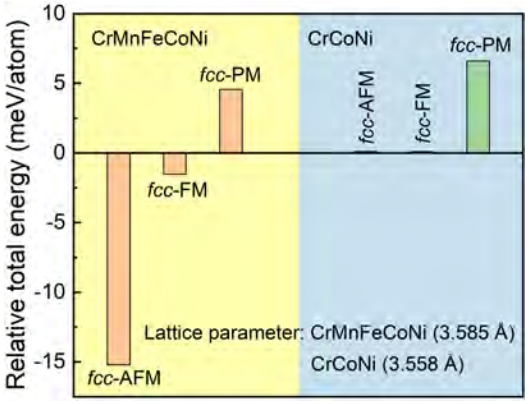

FIG. 4. Calculated total energy for CrMnFeCoNi and CrCoNi HEAs with various magnetic ordering and crystal structures relative to the total energy of the hcp-PM phase. The AFM, FM, and PM refer to the antiferromagnetic state, ferromagnetic state, and paramagnetic state, respectively. The AFM order helps stabilize the fcc phase.

comparison, for the CrCoNi alloy (Fig. 4), the hcp-PM phase always maintains the lowest total energy. This explains the observed fcc-to-hcp transformation during low-temperature deformation [13]. At high temperatures, the fcc phase is stabilized by entropy. Indeed, for CrMnFeCoNi HEA, strong spin fluctuations are observed at room temperature [see Fig. 3(c)], which contributes to the entropy term and hence lowers the Gibbs energy of the fcc structure. This is why a stable fcc phase in CrMnFeCoNi HEA is found over a wide temperature range.

In conclusion, the magnetic behavior of CrMnFeCoNi HEA was investigated by elastic and inelastic neutron scattering. The experimental results showed conclusive evidence of antiferromagnetic ordering below a Néel temperature T_N of ~80 K. The observation of the superlattice peaks plus the development of preferred orientation due to tensile loading has allowed us to propose an antiferromagnetic structure similar to that of γ-Mn for CrMnFeCoNi HEA, with the magnetic moments pointing toward the $\langle 111 \rangle$ direction. The calculated magnetic intensities based on the proposal model are consistent with the neutron scattering results. First-principles calculations have shown that the antiferromagnetic order significantly lowers the total energy of the fcc phase. Meanwhile, strong spin fluctuations were found (by inelastic neutron scattering) to persist up to room temperature in CrMnFeCoNi HEA, a temperature more than three times the T_N. The existence of strong spin fluctuations further stabilizes the fcc phase at high temperatures by increasing the magnetic entropy. These two aspects, together, underpin the relatively high stability for the fcc phase in CrMnFeCoNi HEA.

Acknowledgments—This work is supported by a grant from the Research Grants Council of the Hong Kong Special Administrative Region, China [C1020-21G],

Shenzhen Science and Technology Program (Project No. JCYJ20220818101203007), and the Ministry of Science and Technology of China (Grants No. 2022YFE0109900 and No. 2021YFB3501201). X. L. W. thanks the Croucher Foundation for the Croucher Senior Research Fellowship (CityU Project No. 9509008). S. H. is thankful for the grant support from MEXT Program: Data Creation and Utilization Type Material Research and Development (JPMXP1122684766). H. H. acknowledges the support from the Guangdong Basic and Applied Basic Research Foundation (2023A1515140001) and the Large Scientific Facility Open Subject of Songshan Lake (KFKT2022B08), Dongguan, Guangdong. The elastic and inelastic neutron scattering experiments were carried out at the TAKUMI beamline of J-PARC under proposal No. 2017B0142 and No. 2022L0400 and at the AMATERAS beamline under proposal No. 2018A0176, respectively. This project also benefitted from the use of MPI beamline of China Spallation Neutron Source.

[1] J. W. Yeh, S. K. Chen, S. J. Lin, J. Y. Gan, T. S. Chin, T. T. Shun, C. H. Tsau, and S. Y. Chang, Adv. Eng. Mater. **6**, 299 (2004).
[2] E. P. George, D. Raabe, and R. O. Ritchie, Nat. Rev. Mater. **4**, 515 (2019).
[3] F. X. Zhang, S. Zhao, K. Jin, H. Xue, G. Velisa, H. Bei, R. Huang, J. Y. P. Ko, D. C. Pagan, J. C. Neuefeind, W. J. Weber, and Y. Zhang, Phys. Rev. Lett. **118**, 205501 (2017).
[4] S. Guo, C. Ng, J. Lu, and C. T. Liu, J. Appl. Phys. **109**, 103505 (2011).
[5] M. G. Poletti and L. Battezzati, Acta Mater. **75**, 297 (2014).
[6] G. D. Samolyuk, Y. N. Osetsky, G. M. Stocks, and J. R. Morris, Phys. Rev. Lett. **126**, 025501 (2021).
[7] S. Ghosh, V. Sotskov, A. V. Shapeev, J. Neugebauer, and F. Körmann, Phys. Rev. Mater. **6**, 113804 (2022).
[8] B. Cantor, I. T. H. Chang, P. Knight, and A. J. B. Vincent, Mater. Sci. Eng. A **375–377**, 213 (2004).
[9] G. Laplanche, A. Kostka, C. Reinhart, J. Hunfeld, G. Eggeler, and E. P. George, Acta Mater. **128**, 292 (2017).
[10] M. Naeem, H. He, F. Zhang, H. Huang, S. Harjo, T. Kawasaki, B. Wang, S. Lan, Z. Wu, F. Wang, Y. Wu, Z. Lu, Z. Zhang, C. T. Liu, and X. L. Wang, Sci. Adv. **6**, eaax4002 (2020).
[11] S. Huang, W. Li, S. Lu, F. Tian, J. Shen, E. Holmström, and L. Vitos, Scr. Mater. **108**, 44 (2015).
[12] S. Zhao, G. M. Stocks, and Y. Zhang, Acta Mater. **134**, 334 (2017).
[13] H. He, M. Naeem, F. Zhang, Y. Zhao, S. Harjo, T. Kawasaki, B. Wang, X. Wu, S. Lan, Z. Wu, W. Yin, Y. Wu, Z. Lu, J. J. Kai, C. T. Liu, and X. L. Wang, Nano Lett. **21**, 1419 (2021).
[14] M. Naeem, H. Zhou, H. He, S. Harjo, T. Kawasaki, S. Lan, Z. Wu, Y. Zhu, and X.-L. Wang, Appl. Phys. Lett. **119**, 131901 (2021).
[15] G. Laplanche, A. Kostka, O. M. Horst, G. Eggeler, and E. P. George, Acta Mater. **118**, 152 (2016).
[16] L. Vitos, P. A. Korzhavyi, and B. Johansson, Phys. Rev. Lett. **96**, 117210 (2006).
[17] I. Bleskov, T. Hickel, J. Neugebauer, and A. Ruban, Phys. Rev. B **93**, 214115 (2016).
[18] J. Šebesta, K. Carva, and D. Legut, Phys. Rev. Mater. **3**, 124410 (2019).
[19] C. Niu, C. R. LaRosa, J. Miao, M. J. Mills, and M. Ghazisaeidi, Nat. Commun. **9**, 1363 (2018).
[20] O. Schneeweiss, M. Friák, M. Dudová, D. Holec, M. Šob, D. Kriegner, V. Holý, P. Beran, E. P. George, J. Neugebauer, and A. Dlouhý, Phys. Rev. B **96**, 014437 (2017).
[21] Ö. Özgün, D. Koch, A. Çakır, T. Tavşanoğlu, W. Donner, M. Farle, and M. Acet, Phys. Rev. B **106**, 214422 (2022).
[22] K. Jin, B. C. Sales, G. M. Stocks, G. D. Samolyuk, M. Daene, W. J. Weber, Y. Zhang, and H. Bei, Sci. Rep. **6**, 20159 (2016).
[23] See Supplemental Material at http://link.aps.org/supplemental/10.1103/PhysRevLett.133.126701 for result of composition analysis, experimental setup for the neutron diffraction experiments during tensile loading, additional results of elastic and inelastic neutron scattering, and simulated neutron powder diffraction patterns of different magnetic structure models.
[24] K. Nakajima *et al.*., J. Phys. Soc. Jpn. **80**, SB028 (2011).
[25] R. T. Azuah, L. R. Kneller, Y. Qiu, P. L. Tregenna-Piggott, C. M. Brown, J. R. Copley, and R. M. Dimeo, J. Res. Natl. Inst. Stand. Technol. **114**, 341 (2009).
[26] L. Vitos, Phys. Rev. B **64**, 014107 (2001).
[27] L. Vitos, *Computational Quantum Mechanics for Materials Engineers: The EMTO Method and Applications* (Springer Science & Business Media, New York, 2007).
[28] J. P. Perdew, K. Burke, and M. Ernzerhof, Phys. Rev. Lett. **77**, 3865 (1996).
[29] B. Gyorffy, A. Pindor, J. Staunton, G. Stocks, and H. Winter, J. Phys. F Met. Phys. **15**, 1337 (1985).
[30] S. Mugiraneza and A. M. Hallas, Commun. Phys. **5**, 95 (2022).
[31] R. J. Birgeneau, R. A. Cowley, G. Shirane, H. Yoshizawa, D. P. Belanger, A. R. King, and V. Jaccarino, Phys. Rev. B **27**, 6747 (1983).
[32] A. S. Stefanescu and P. J. Becker, J. Phys. C **14**, L737 (1981).
[33] Y. Ishikawa, M. Kohgi, and Y. Noda, J. Phys. Soc. Jpn. **39**, 675 (1975).
[34] Y. Ishikawa and Y. Endoh, J. Phys. Soc. Jpn. **23**, 205 (1967).
[35] E. Fawcett, Rev. Mod. Phys. **60**, 209 (1988).
[36] G. Shirane, Acta Crystallogr. **12**, 282 (1959).
[37] L. A. I. Kestens and H. Pirgazi, Mater. Sci. Technol. **32**, 1303 (2016).
[38] Z. R. Wang, X. L. Wang, J. A. Fernandezbaca, D. C. Johnston, and D. Vaknin, Science **264**, 402 (1994).
[39] G. L. Squires, *Introduction to the Theory of Thermal Neutron Scattering* (Dover Publications, New York, 1996).
[40] B. H. Toby and R. B. Von Dreele, J. Appl. Crystallogr. **46**, 544 (2013).
[41] M. E. McHenry, M. A. Willard, and D. E. Laughlin, Prog. Mater. Sci. **44**, 291 (1999).
[42] D. Ma, B. Grabowski, F. Körmann, J. Neugebauer, and D. Raabe, Acta Mater. **100**, 90 (2015).